Natural, Biocompatible, and 3D-Printable Gelatin Eutectogels Reinforced with Tannic Acid Coated Cellulose Nanocrystals for Sensitive Strain Sensors

Journal:	*ACS Applied Electronic Materials*
Manuscript ID	el-2023-000755.R1
Manuscript Type:	Article
Date Submitted by the Author:	n/a
Complete List of Authors:	Mercadal, Pablo; IPQA (CONICET-UNC); National University of Cordoba Romero, Marcelo; IPQA (CONICET-UNC); National University of Cordoba Montesinos, Maria del Mar; Centro de Investigaciones en Bioquímica Clínica e Inmunología; National University of Cordoba Real, Juan ; National University of Cordoba Picchio, Matias; IPQA (CONICET-UNC), Polymer chemistry Gonzalez, Agustin; IPQA (CONICET-UNC); National University of Cordoba

SCHOLARONE™
Manuscripts

Natural, Biocompatible, and 3D-Printable Gelatin Eutectogels Reinforced with Tannic Acid-Coated Cellulose Nanocrystals for Sensitive Strain Sensors

Pablo A. Mercadal[a]; Marcelo R. Romero[a]; Maria del Mar Montesinos[b]; Juan Pablo Real[c]; Matias L. Picchio[d,e]* and Agustín González[a]*

[a] Departamento de Química Orgánica, Facultad de Ciencias Químicas (Universidad Nacional de Córdoba), IPQA−CONICET, Medina Allende y Haya de la Torre, Córdoba 5000, Argentina

[b] Departamento de Bioquímica Clínica, Facultad de Ciencias Químicas (Universidad Nacional de Córdoba), Centro de Investigaciones en Bioquímica Clínica e Inmunología (CIBICI-CONICET), Medina Allende y Haya de la Torre, Córdoba 5000, Argentina

[c] Unidad de Investigación y Desarrollo en Tecnología Farmacéutica (UNITEFA-CONICET), Universidad Nacional de Córdoba, Medina Allende y Haya de la Torre, Córdoba 5000, Argentina

[d] Instituto de Desarrollo Tecnológico para la Industria Química (INTEC-CONICET), Güemes 3450, Santa Fe 3000, Argentina.

[e] POLYMAT, Applied Chemistry Department, Faculty of Chemistry, University of the Basque Country UPV/EHU, Paseo Manuel de Lardizabal 3, Donostia-San Sebastián 20018, Spain

*Corresponding authors

Agustín González: agustingonzalez@unc.edu.ar

Matias L. Picchio: mlpicchio@santafe-conicet.gov.ar

1
2
3
4
5
6
7
8
9
10
11
12
13
14
15
16
17
18
19
20
21
22
23
24
25
26
27
28
29
30
31
32
33
34
35
36
37
38
39
40
41
42
43
44
45
46
47
48
49
50
51
52
53
54
55
56
57
58
59
60

Abstract

Ionic gels from eutectic mixtures are attracting extensive interest in bioelectronics owing to their nonvolatile nature, low cost, and inherently high ionic conductivity. Biodegradable electronics made of biopolymers envisage a promising future in this field, but unfortunately, they often feature poor mechanics. Herein, we explored tannic acid-decorated cellulose nanocrystals (TA@CNC) as dynamic nanofillers of biocompatible eutectogels based on gelatin and a eutectic mixture composed of choline chloride and ethylene glycol (ethaline). Small concentrations of TA@CNC (up to 1−2 wt%) allow increasing by two-fold the strength (30 kPa) and stretchability (180%) of the eutectogels while improving their ionic conductivity (105 mS·m^{-1}). The reversible physical network of the protein and multiple hydrogen bonding interactions with tannic acid endow these eutectogels with good self-adhesiveness, suitable gel-to-sol transition for 3D printing, and recyclability. We further used the cellulose nanocomposite eutectogels as skin-conformal electrodes for monitoring different motions of the human body with excellent sensitivity in the open air thanks to the low volatility of ethaline. All in all, these results demonstrate a facile strategy to boost the properties of biopolymer eutectogels using inexpensive and renewable raw materials as rigid nanoreinforcers.

Keywords: Eutectogels, Tannic Acid, Cellulose Nanocrystals, Motion sensor, 3D printing.

Introduction

Eutectic mixtures and deep eutectic solvents (DES) have recently emerged as low-cost electrolytes for a myriad of technological applications.[1,2] Shearing many features of costly ionic liquids (ILs), such as low vapor pressure, high ionic conductivity, and good thermal stability, eutectic mixtures offer fresh opportunities for designing adaptive materials.[3] The immobilization of eutectic solvents into polymer supports renders soft ionic materials called eutectogels that are being actively developed for healthcare monitoring, bioelectrodes, wearable sensors, and other biomedical applications.[4,5] In this vein, eutectogels from synthetic polymers, such as poly(vinyl alcohol),[6,7] poly(acrylic acid),[8–11] poly(acrylamide),[12,13] poly(1-vinylimidazole),[14] and waterborne polyurethane,[15,16] have found multiple applications recently. These materials highlight mechanical robustness but are not degradable; their biocompatibility is often compromised and can not be recycled in most cases.

Alternatively, natural polymers with intrinsic biocompatibility and biodegradability are more appealing for constructing functional eutectogels in applications requiring skin contact[17,18] and degradable electronic devices.[19,20] Unluckily, biopolymer eutectogels commonly suffer from poor mechanical properties that have hampered the growth of the biodegradable electronics realm, finding only a few examples of these materials in the literature. For instance, injectable eutectogels were prepared from guar gum or xanthan gum and several natural deep eutectic solvents (NADES).[21–23] Yan et al. reported lignin eutectogels supporting a ternary eutectic mixture of choline chloride (ChCl)/urea/ glycerol as a template to fabricate

hierarchical porous carbons for supercapacitors.[24] More recently, sodium alginate was combined with binary NADES comprising proline, glucose, and sorbitol to produce food-protecting anti-frosting eutectogels.[25]

Panzer *et al*. have pioneered gelatin eutectogels using the eutectic mixture of ChCl and ethylene glycol (EG) (1: 2 molar ratio), the so-called ethaline.[26,27] At this point, it is worth mentioning that recent studies have proved that ethaline behaves as an ideal mixture and consequently can not be considered a DES but simply a classical eutectic system.[28,29] The gelatine/ethaline eutectogels showed unsatisfactory ultimate tensile strength and fracture strain of 0.8 kPa and 54% for a protein concentration of 12 wt%. Therefore, rationale approaches for improving the mechanical robustness of biopolymer eutectogels are constantly being sought to expand their applicability as gel electrolytes.[30]

In this sense, tannic acid-coated cellulose nanocrystals (TA@CNC) are an excellent option for enhancing the mechanical performances of composites as biobased nanofillers owing to their rigid crystalline core, H-bond forming ability of the natural polyphenol, and high surface area. Indeed, TA@CNC have already demonstrated their outstanding reinforcer capacity in several nanocomposite hydrogels.[31–34] Interestingly, tannic acid has shown an extraordinary binding affinity for proteins, and a superior reinforcing performance could be expected for TA@CNC compared to pristine CNC.[35–38]

Herein, we propose for the first time the use of TA@CNC as a simple strategy to modify and control the mechanical and viscoelastic behavior of gelatin/ethaline eutectogels (BioeGels). The extraordinary hydrogen bonding capability of TA@CNC

allows excellent dispersibility in ethaline and superb interaction with the protein. This fact, along with the physical gelatin network by triple helix formation, affords thermoreversible yet resilient eutectogels with great promise for direct ink writing of soft electronics. The nanocomposite BioeGels showed good mechanical strength, stretchability, self-adhesiveness, stable viscoelastic behavior, compression resistance, high ionic conductivity, and non-toxicity in a human fibroblast cell line. Furthermore, the BioeGels were evaluated as strain sensors, displaying good sensitivity and high stability in the open environment.

Materials and Methods

Materials: Ethylene glycol (EG, Cicarelli, ≥95.5%); Choline Chloride (Sigma Aldrich, ≥99%); Gelatin from porcine skin Type A (Sigma Aldrich, gel strength ~300 g Bloom); CNC (CelluForce NCV100, diameter: 2.3−4.5 nm, length: 44−108 nm, surface area 5.5×10^{20} nm^2/g) and tannic Acid (Bio Pack, ≥99%) were used as received without any further purification. Deionized water was used throughout the work.

Methods

Preparation of TA@CNC

CNC coated with TA were prepared according to Carnicero *et al*.[33] Briefly, 1 g of CNC was dispersed in 100 mL of distilled water using magnetic stirring and sonicated for 10 min. Then, the pH of the dispersion was adjusted to 8, using Tris buffer (1 M). Finally, 3 g of TA was added to the dispersion and stirred magnetically for 12 h. The TA@CNC was stored at 4 °C until lyophilization. Before use, the

powder was mechanically ground with a mortar obtaining a final yield of 87% w/w. Note that the surface area of CNC provided by the supplier's datasheet is 4×10^{20} nm^2/g, whereas the surface area of tannic acid is 7.78 $nm^2/molecule$[39], giving 8.26×10^{21} $nm^2/3$ g. Therefore, the entire CNC surface area is expected to be covered with TA molecules.

Preparation of Ethaline

To prepare 100 g of ethaline (ChCl: EG, 1: 2 molar ratio), 52.9 g of ChCl was dissolved in 47.1 g of EG at 90 °C under magnetic stirring until a homogeneous liquid was formed.[40]

Synthesis of BioeGels

BioeGels loaded with 1, 2, and 4 wt% of TA@CNC were prepared. Initially, 1.8 g of gelatin was dissolved in 16.02, 15.84, and 15.48 g of ethaline at 90°C under magnetic stirring. Then, 0.18, 0.36, and 0.72 g of TA@CNC were added to the mixture to obtain BioeGels with 1 (BioeGel1%), 2 (BioeGel2%), and 4 wt% (BioeGel4%) of TA@CNC, respectively. Once the gelatin was completely dissolved, the dispersions were poured into 10×10 cm silicone molds and cooled at 4°C for 24 h. The control sample was prepared without adding TA@CNC (BioeGel0%). In all cases, the gelatin concentration was 10 wt%.

Swelling test

The water uptake ($\%S$) of the different samples was calculated according to the following expression:[41]

$$\%S = [(W_s - W_0)/W_0] \times 100 \tag{1}$$

where W_0 is the initial weight of the samples and W_s the weight after immersion in 30 mL of deionized water for specific time intervals at room temperature. The W_s values were recorded after removing the samples from the swelling medium and wiping them with tissue paper to absorb the excess water on the surfaces. All measurements were performed in triplicate.

Thickness determination

BioeGels thickness was determined as the average of 10 measurements for each sample using a hand-held micrometer (model ESP1-0001PLA, Schwyz, Swiss). The average thickness was used for assessing mechanical properties. The thickness of the as-prepared BioeGels had average values of 775 ±32, 793 ±47, 703 ±70, and 685 μm ±34 for BioeGel0%, 1%, 2%, and 4%, respectively.

FTIR analysis

The BioeGels were characterized by attenuated total reflectance-Fourier transform infrared spectroscopy (ATR-FTIR) using a Nicolet 5-SXC spectrometer coupled to a Nicolet iN10 microscope (Thermo Scientific, USA) and a ZnSe crystal with an incidence angle of 45°. Spectra were recorded in reflection mode by depositing the sample on a gold mirror and collected as an average of 32 scans with 4 cm^{-1} resolution and air as the background. Different areas of the BioeGels were analyzed to confirm the homogeneity of each sample.

Morphological Characterization

The surface morphology of the different BioeGels was studied by scanning electron microscopy (SEM). Lyophilized BioeGels were attached to a double-sided carbon

adhesive tape mounted on SEM stubs, coated with chrome under vacuum, and examined with an SEM microscope (Carl Zeiss - Sigma, Germany). SEM images were acquired at a magnification of 500x, an aperture size of 30 μm, electron high tension (EHT) of 3 kV, and a working distance of 4 mm.

Atomic force microscopy (AFM) height images of CNC and TA@CNC were acquired using a commercial Agilent Technology 5500 Scanning Probe Microscope operating in tapping mode. The measurements were conducted in acoustic mode at room temperature using a standard Si_3N_4 cantilever with a resonant frequency of 145-230 kHz. 2 × 2 µm - pixel resolution. The AFM images were collected at a scanning rate of 0.3 line.s^{-1}. The sample was prepared by drop casting on glass.

Dynamic Light Scattering

The hydrodynamic diameter of the TA@CNC dispersion was determined by dynamic light scattering (DLS) at room temperature using a Nano Zetasizer instrument (Malvern Panalytical, UK) with a He–Ne laser (λ = 633 nm) and scattering angle of 173°.

Mechanical properties

The mechanical properties of the BioeGels were determined by tensile, compression, and relaxation tests. For the tensile assay, the samples were cut using a steel template with bone shape according to ASTM D882-02 standard method[42] and subjected to controlled deformations, collecting the record of the stress-strain curves. Initial separation of 45 mm and a crosshead speed of 25 mm·min^{-1} were used. Toughness values for BioeGels were calculated from the area under stress vs. strain curves.

Stress relaxation measurements were carried out with a constant strain of 80% for 300 s, and the time-dependent stress was recorded.

Compression tests were performed at a constant speed of 18 mm.min^{-1} and up to maximum deformation of 80% on cylindrical samples of 1.2×1 cm in diameter and height, respectively. All tests were performed in quintuplicate on an Instron Universal Testing Instrument (model EMIC 23-5S, Norwood, MA, USA) equipped with a 50 N load cell.

Adhesiveness test

Adhesive stress measurements were performed at room temperature using an Instron Universal Testing Instrument (model EMIC 23-5S, Norwood, MA, USA) equipped with a 5 N load cell. Samples of 30×1 mm in diameter and thickness, respectively, were placed with an epoxy adhesive in the moving cell grid of the instrument. Then, the moving cell was moved slowly towards a fixed porcine skin portion, and a pressure of 5 N was applied for 1 min. The adhesive strength was calculated from the force recorded while detaching the BioeGels from the skin, using a crosshead speed of 0.05 mm·s-1. The tackiness and adhesion energy of the BioeGels were calculated from the maximum force needed to pull apart the sample and the area under the stress−strain curve during the probe-removing stage, respectively. This procedure was subsequently conducted in 5 cycles to study the adhesion repeatability. In addition, proof adhesion tests were performed on other surfaces such as Teflon, steel, wood, polypropylene, and glass. The reported values correspond to the average of three measurements of the same sample.

3D printing test

Using a computer-aided design platform (www.onshape.com), a 3D geometric design consisting of a rectangular grid with a perimeter of 20 × 10 mm and a height of 1.5 mm formed by 3 layers, each one of 0.5 mm, was made to print. In order to obtain the mesh of the grid, the filling density of the internal network was set at 50%, and filaments of even layers were arranged at 45° to the filaments of uneven layers. The design, in STL file format, was loaded to the Repetier Host software (Repetier-Host V 2.1.3), which was used to create the rectangular design internal structure and obtain the instruction code (g-code) that the printer would follow. The dosage forms consisted of a shell with a thickness of 500 μm and a rectilinear internal network of the same material.

The 3D-printed BioeGels were obtained using Melting Solidification Printing Process (MESO-PP), loading the samples in conventional plastic syringes of 1 mL. The printer was a 3-Donor® developed by Life SI, and the printing parameters were the following: print head temperature: 37 °C; platform temperature: 25 °C; the amount of material per point: 10 nL; printing pressure: 0.02 bar; layer printing delay: 1200 ms.

The quality of the 3D-impressed BioeGels was studied in terms of irregularity (I) and pore printability (P_p).[43] I of a scaffold specifies the overall accuracy of the printed scaffold in comparison to its design in terms of outer geometry, but not internal structure; whereas, P_p is complementary as it focuses on the internal scaffold geometry. I can be defined according to the following expression:

$$I_{(X;Y;Z)} = \frac{Experimental\ length_{(X;Y;Z)}}{Design\ length_{(X;Y;Z)}} \times 100 \tag{2}$$

where $Experimental\ length$ is the external dimension of the scaffold after printing and $Design\ length$ is the design dimensions along the X, Y or Z direction. P_p can be calculated as:

$$P_p = \frac{(perimeter\ of\ pore)^2}{16\ \times area\ of\ pore} \tag{3}$$

where $perimeter\ of\ pore$ and $area\ of\ pore$ are calculated measuring the perimeter and area of each pore in a scaffold structure and then averaging the values of all pores presents in the 3D printed structure.

Rheological tests

Rheological tests were performed using an Anton Paar rotational rheometer (Physica MCR 301, Austria). A parallel plate geometry of 8 mm in diameter was used for the different tests. Amplitude sweeps were carried out to determine the linear viscoelastic range (LVR) of BioeGels samples at 20°C with a frequency of 1 Hz and strain amplitude from 0.1 to 100%. For frequency sweeps, a fixed strain of 1% was selected with a varied frequency interval from 0.1 to 100 Hz at 20°C. Dynamic mechanical thermal analysis (DMTA) was performed at a strain of 1% and a frequency of 1 Hz, while the temperature was varied from 0 to 100 °C.

Movement sensor

The test was designed considering the movement of the index finger flexion-extension with respect to the back of the hand before (5°) and after (90°) grasping a small ball, according to Chen et al. studies.[44]

BioeGels resistivities were tested during a repeated flexural deformation process using a servomotor (sg90, China) electronically controlled by an Arduino Uno microcontroller (Italy) and mechanically supported by 2 sections of a 3D printed PLA platform of 2 × 5 cm each (Duplicator 3D mini, China and Wanhao-Cura 18.05 software). This structure has a hinge shape that simulates the index finger's flexion with a bending angle from 5° to 90° into a close loop of 12 s period. A pair of 2.0 × 0.5 cm rectangular gold electrodes were fixed to the printed platform at 2.5 cm of flexion region and with a linear distance of 5 cm between them. In a previous step, each BioeGel was cut into a rectangular shape of a mean size of 2 × 6.7 cm, placed onto the platform, and pressed over gold electrodes to promote electronic contact. The electrodes were connected to a digital multimeter (UNI-T UT71C, UNI-TREND, China), and resistance over time was registered with a digital interface RS232 and data logger software. Before the assay, the accurate dimensions and thickness of BioeGels were measured using a hand-held micrometer (model ESP1-0001PLA, Schwyz, Swiss).

The specific conductivity (k) was calculated from resistance data according to the following expression:

$$k = \frac{1}{R} \times \frac{L}{A} \qquad (4)$$

where A is the transversal BioeGel area (width × thickness, m^2), R resistance (ohms), and L the distance between the gold electrodes (m), respectively. All measurements were performed in triplicate.

1
2
3
4
5
6
7
8
9
10
11
12
13
14
15
16
17
18
19
20
21
22
23
24
25
26
27
28
29
30
31
32
33
34
35
36
37
38
39
40
41
42
43
44
45
46
47
48
49
50
51
52
53
54
55
56
57
58
59
60

In vitro cytotoxicity study

The cytotoxicity of BioeGels extracts towards cells was analyzed using methyl thiazolyl tetrazolium (MTT) assay in accordance with the International Organization for Standardization (ISO) 10993-5 and ISO 10993-12 on MRC-5 human fibroblast cells.[45,46] MRC-5 cells from American Type Culture Collection (ATCC CCL-171) were cultured in Dulbecco's modified Eagle's medium (DMEM, Gibco, USA) supplemented with 10% fetal bovine serum (FBS, Gibco), 100 units·mL^{-1} penicillin, and 100 µg·mL^{-1} streptomycin, in a humidified atmosphere of 5% CO_2/ 95% air at 37°C. The BioeGels (0, 1, 2, and 4 wt%) were sterilized under UV light for 30 min, and then 20 mg were incubated into 10 mL of DMEM-10% FBS at 37°C for 24 h. MRC-5 cells seeded on 48-well plates at 70-80% confluence were exposed to varying concentrations (25, 50, 75, and 100 %) of BioeGels extracts for 24 h, and their viability was evaluated by MTT assay.[47] Fresh MTT (Sigma-Aldrich, USA) solution in Phosphate-buffered saline (PBS) was prepared in a stock concentration of 5 mg/ml and further diluted in DMEM to reach a 10% MTT solution. The MTT solution was added into each well for 4 h incubation at 37°C, and the culture supernatant was discarded. Dimethyl sulfoxide (DMSO, 80 µl) was added to each well and gently mixed until completely dissolve the formazan crystals. The optical density (OD) was measured at 570 nm using a Microplate Reader (BIO-RAD, USA). The percentage of viable cells was calculated as follows:

$$Cell\ viability = \frac{OD_{570}BioeGel}{OD_{570}Control} \times 100 \tag{5}$$

where OD_{570} BioeGel and OD_{570} Control are de OD for cells cultured in BioeGels extracts and DMEM, respectively. The experiments were conducted in triplicate.

Biodegradability Test

Biodegradation experiments were carried out according to the protocol described by González *et. al*[48] and performed in triplicate. In a closed environment, equal masses of each BioeGel were buried in a characterized soil for 6 days. The most relevant physicochemical properties of the soil were: organic matter: 10%; organic carbon: 5.80%; total nitrogen: 0.464%; C/N ratio: 12.5; nitrates: 128.0 ppm; sulfates: 23.3 ppm; phosphorus: 58.7 ppm; pH: 7.14 and electrical conductivity of saturation extract: 3.1 dS/m. The samples were cut into circular pieces, dried in an oven at 105 °C for 12 h, and weighed (W_i). The films were then buried into an iron mesh (to allow access to moisture and microorganisms and to facilitate the removal of the degraded samples) in plastic boxes at a depth of 8 cm from the soil surface. The assay was performed at (22±3) °C and (42±4) RH by adding water periodically. Fluctuations in soil moisture were followed gravimetrically using the standard oven drying method. Samples were taken from the soil after 6 days of incubation and cleaned by wiping gently with a soft brush. Then, the samples were dried in an oven at 105 °C for 12 h and weighed (W_f) to assess the average % of weight loss according to Eq 6:

$$\% \text{ Weigth Loss } = \left(\frac{W_i - W_f}{W_i}\right) \times 100 \tag{6}$$

**Statistical analysis**

Data for each test were statistically analyzed. The analysis of variance (ANOVA) was used to evaluate the significance of the difference between means. Turkey test was used for comparing mean values; differences between means were considered significant when $P \leq 0.05$.

Results and Discussion

The BioeGels were prepared through a simple process involving the dissolution of gelatin in ethaline at high temperature, the dispersion of TA@CNC, and the cooling of the mixture at 4°C to induce the formation of gelatin triple helices and create a physical network (Scheme 1). BioeGels without TA@CNC were transparent, while as the TA@CNC content is increased from 1 to 4 wt%, the eutectogels exhibited a color change from yellowish to brownish, respectively. The gels' transparency indicates a good dispersibility of TA@CNC, where multiple H-bond interactions with ethaline and the protein avoid extensive aggregation of nanocrystals.
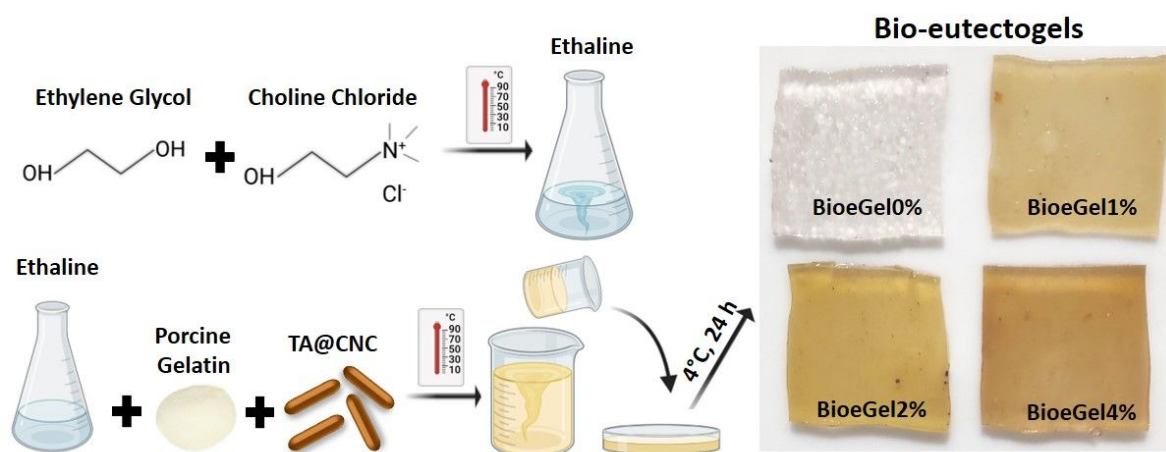
Scheme 1. Schematic illustration of the 2-step process to obtain the BioeGels loaded with different % of TA@CNC.

TA@CNC were characterized by DLS and AFM. The DLS reveals that TA@CNC has a unimodal particle size distribution with Z-average and PDI values of around 72 nm and 0.307, respectively (Figure 1A). Note that the DLS technique determines the hydrodynamic diameter of the TA@CNC in the dispersion based on the assumption that the particles have a spherical shape. AFM image of CNC (Figure 1B i) shows a

filament morphology and a homogeneous particle distribution. After coating the CNC

with TA, the AFM image of TA@CNC show similar morphological features ruling out

the formation of nanoparticle agglomerates (Figure 1B ii).
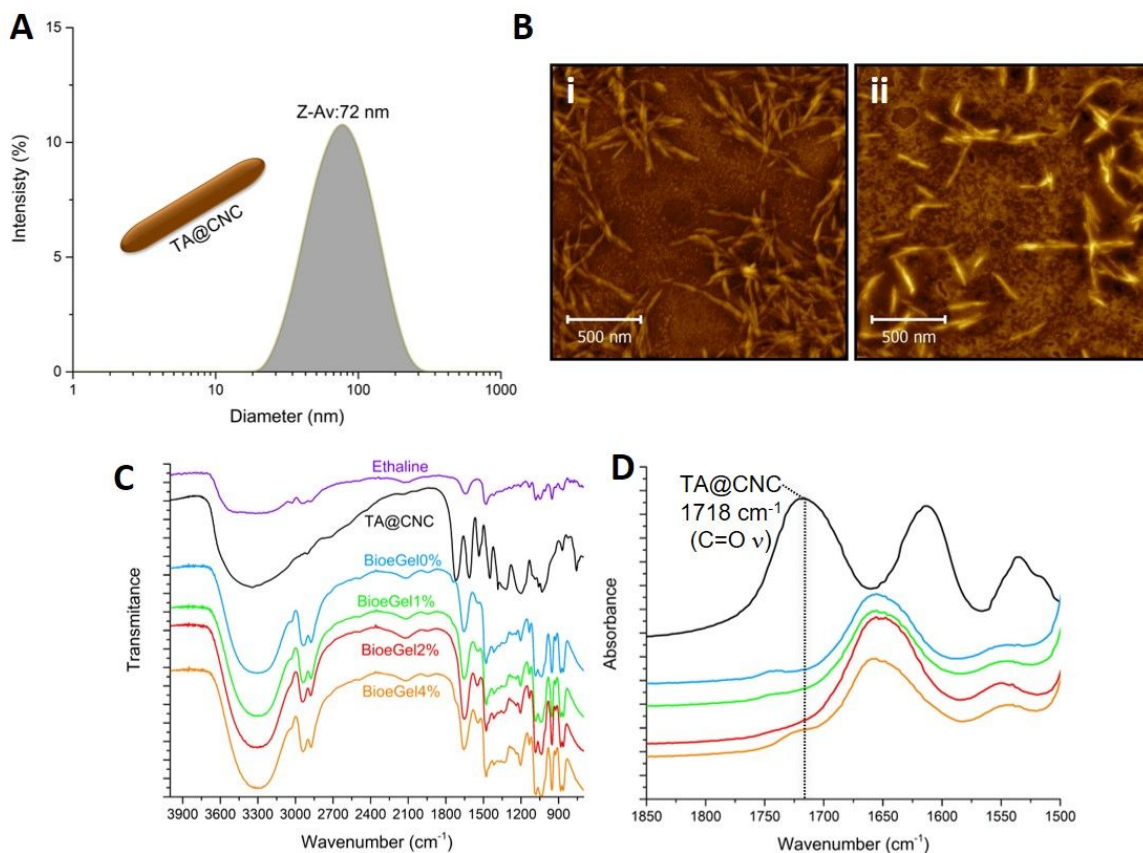
Figure 1. A) Particle size distribution of TA@CNC determined by DLS. **B)** AFM phase images (2000 × 2000 nm) of the CNC (i) and TA@CNC (ii). **C)** FTIR spectra of BioeGels and pure Ethaline and TA@CNC. **D)** FTIR spectra of BioeGels and TA@CNC in the range of 1900-1400 cm^{-1}.

The chemical characterization of the BioeGels and TA@CNC was performed by

ATR-FTIR spectroscopy. As shown in Figure 1C purple line, ethaline shows

characteristic vibrational modes at 3500-3200 cm^{-1}(O-H ν), 3200-2800 cm^{-1} (C-H ν),

strong peaks at 1482 cm^{-1} (CH$_2$ δ, CH$_3$ δ as) and 1414 cm^{-1} (CH$_3$ δ sy), 1260–970

cm^{-1} range (C-O ν), and 1082 cm^{-1} (C-N ν).[49,50] Figure 1C black line illustrates the

IR spectrum of TA@CNC, where the broad absorption band at 3000−3700 cm$^{−1}$ is

attributed to the O−H ν of TA and CNC. Also, vibrational modes at 1100−900 cm$^{−1}$

can be appreciated and assigned to C−O−C vibrations of CNC. Typical bands of TA

at 1701 (C=O ν); 1607, 1535, and 1448 cm$^{−1}$ (aromatic C−C skeletal vibrations); and

870 and 755 cm$^{−1}$ (aromatic C−H δ oop, C=C δ) are slightly bathochromic shifted,

indicating that TA is coating the CNC.[33]

The IR bands of ethaline can be appreciated in all BioeGels spectra due to its

relatively high concentration (Figure 1C). The band at 3500-3000 cm^{-1} in the

BioeGels spectra is more intense than in ethaline/TA@CNC spectra due to the

contribution of Amide A (N-H ν) from gelatin. Besides, the vibrational modes of

Amide I, Amide II, and Amide III of porcine gelatin are observed at 1650 (C=O ν),

1549 (NH δ ip and N-C=O ν sy), and 1240 cm^{-1}, respectively.[51] BioeGels spectra are

similar, and no changes in the intensity of the TA@CNC modes were observed as

the concentration increased. However, the band at 1718 cm^{-1} (C=O ν) in TA@CNC

(Figure 1D, black line) can be observed as a shoulder in BioeGels4% (Figure 1D,

orange line) while for other TA@CNC concentrations, it is not appreciated due to its

the small amount.

The morphological characterization of the BioeGels was performed by acquiring

SEM images of previously lyophilized circular samples. After the drying process,

BioeGels keep their shape and show rough surfaces whose color varies from white

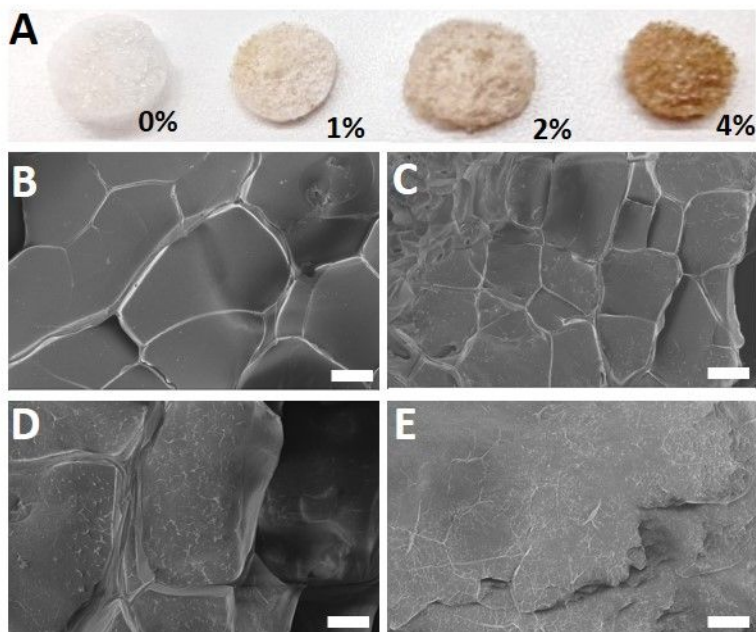to yellow-brown as the concentration of TA@CNC increases (Figure 2A).

Figure 2. Photography of lyophilized BioeGels with different content of TA@CNC (**A**) and SEM images of BioeGel0% (**B**), BioeGel1% (**C**), BioeGel2% (**D**) and BioeGel4% (**E**). Scale bars = 20 μm.

SEM image of BioeGel0% exhibits a surface with defined flake-shaped cracks, whose inside is smooth and clean (Figure 2B). With the addition of TA@CNC, rod-shaped nanoparticles within the flakes start to appear in BioeGel1% (Figure 2C), while for BioeGels2%, the presence of these nanocrystals is more noticeable (Figure 2D). Interestingly as shown in Figure 2E, unlike the other eutectogels, for BioeGel4% the high quantity of TA@CNC hides the defined flake-shaped cracks, and the uniform distribution of nanocrystals in the material becomes highly notorious. Note that the presence of rod-shaped TA@CNC observed in the SEM images keeps a shape correlation with the AFM micrography shown in Figure 1B.

Then, we studied the role of TA@CNC on the mechanical properties of the BioeGels by tensile, compression, and relaxation tests (Figure 3). An illustrative picture of the

tensile test for BioeGel0% is shown in Figure 3A. The stress vs. strain curves for the

BioeGels are shown in Figure 3B. Before the addition of TA@CNC, BioeGels0%

have tensile strength and elongation at break values of 10 kPa and 91%, respectively
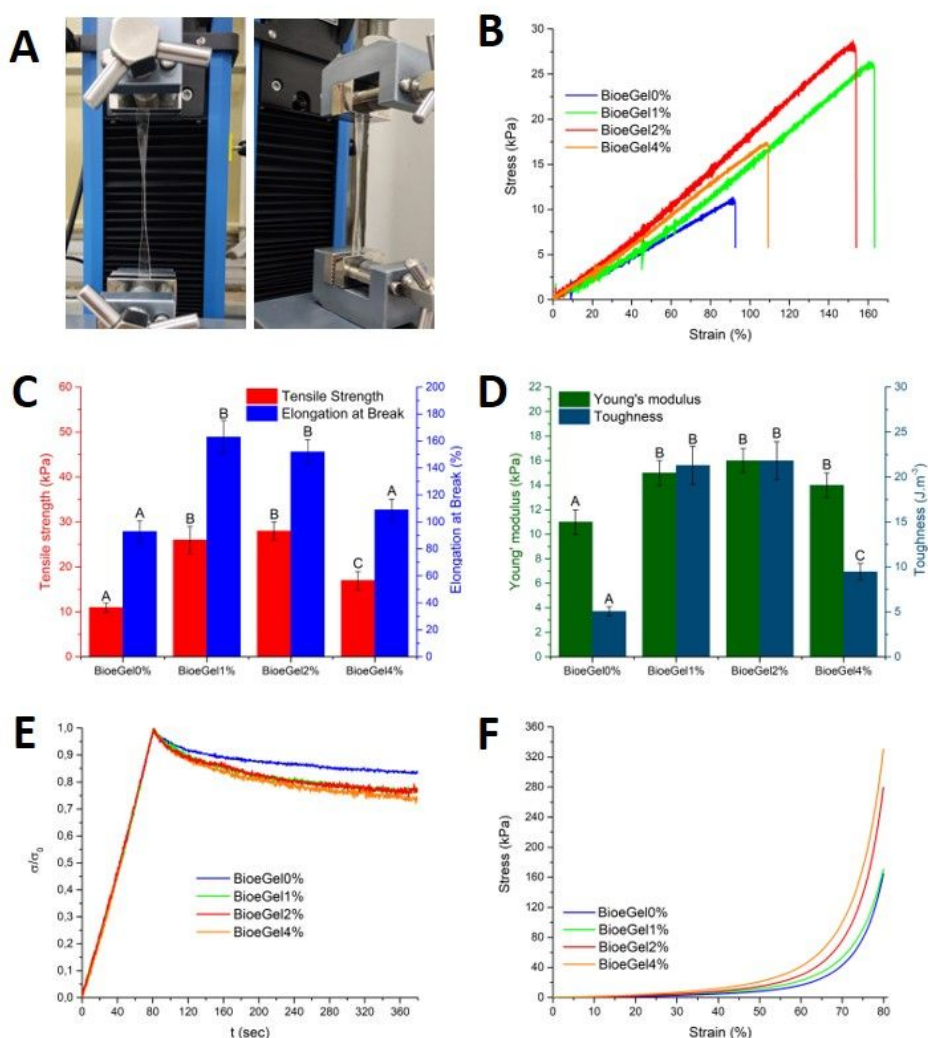
(Figure 3B, C).

Figure 3. A) Photograph of the tensile test of BioeGel0%. **B)** Stress versus strain curves of the prepared BioeGels. **C)** Tensile strength (red column) and Elongation at beak (blue column) values of BioeGels. **D)** Young's modulus (green column) and Toughness (greenish blue column) values of BioeGels. **E)** Stress relaxation curves for BioeGels over time. σ_0 is the maximum stress. **F)** Stress vs. strain compression curves for the BioeGels. All measurements were performed in triplicate. Two values in the same column followed by the same letter are not different ($p \geq 0.05$) according to the Tukey test.

Interestingly, as shown in Figure 3B (green, red, and orange curves), adding even small amounts of TA@CNC improves the stretchability and strength of the BioeGels considerably due to both the reinforcer effect of the rigid CNC core as well as multiple dynamic interactions provided by TA, forming a more robust physically crosslinked network. However, a nonlinear relationship was observed between the TA@CNC content and tensile strength and elongation at break. For instance, BioeGel1% and 2% have similar average values of the tensile strength (26 ± 3 and 28 ± 2 kPa) and elongation at break (163% ± 12 and 153% ± 9), but then these parameters decrease to 17 ± 2 kPa and 109% ± 8 for BioeGel4% turning it a less resistant material (Figure 3C). Young's modulus and toughness follow a similar trend, and nanocrystal contents of 1 and 2 wt% seem to be optimal to maximize the materials' resilience (Figure 3D). The reasons for the mechanical detriment when using 4 wt% of TA@CNC could be associated with some nanocrystal agglomerations, as shown in Figure 2E, impairing their reinforcing mechanism relying on interfacial debonding. Similar results were observed by Wiesenborn *et al.* for PEO films prepared with different concentrations of CNC.[52] Although the mechanical performance of recently reported chemically crosslinked synthetic eutectogels is superior to that of BioeGels, the stretchability and strength of these biobased nanocomposites are high enough to allow their application as motion sensors, with the advantages of biocompatibility and biodegradability that natural polymers offer.

Stress relaxation tests were performed to study the dynamic structural rearrangement of the BioeGels at different contents of TA@CNC setting an

elongation strain of 80%. As shown in Figure 3E, the addition of TA@CNC led to a faster release of stress in the nanocomposites than BioeGel0%. Furthermore, a slight increase in the stress relaxation rate was observed when incorporating 4 wt% of TA@CNC (Figure 3E, orange curve). These results reveal the superior ability of the nanocomposite eutectogel network to undergo rearrangement by H-bonds interactions between TA@CNC skeleton and gelatin chains, providing significant energy dissipation by reversible association and dissociation.[32]

On the other hand, compression tests showed that the compressibility behavior of BioeGels improves linearly after incorporating growing concentrations of TA@CNC (Figure 3F). Here again, the reinforcement effect of TA@CNC is observed, and BioeGel4% supports the greatest compression stress.

Given the multiple H-bonding abilities of ethaline, TA@CNC, and amino acid residues of gelatin, the BioeGels featured excellent self-adhesiveness, which is a key-sought requirement in skin-conformal sensors. Adhesion tests on porcine skin were performed to study this fundamental property. The tackiness and adhesion energy can be calculated as the maximum stress and the area under the adhesive stress vs. strain curves, respectively. Figure 4A displays the different adhesive stress vs. strain profiles, revealing an increase in the materials' tackiness with the amount of TA@CNC added. Figure 4B, red and blue columns, represent this increasing tendency of tackiness and energy of adhesion.[53] This trend is reasonably expected because the TA that coats the CNC promotes H-bonding formation and thus enhances the adhesion energy values.[33]

Although the tackiness values of BioeGels are lower than those of recently reported gelatin eutectogels[54] but higher than CNC nanocomposite hydrogels,[33,53] the magnitude of the adhesion force of our ionic materials is good enough to be able to adhere to human skin.[55,56] Figure 4C shows the cyclic adhesion test on porcine skin for the most sticky gel, BioeGel4%, observing an adhesion increase with successive cycles. This adhesion improvement could be because, in each cycle, the BioeGel4% was compressed for 1 min producing a migration of ethaline toward the BioeGel surface, favoring the availability of functional groups for H-bonding interactions. Note that this effect is less pronounced when increasing the amount of TA@CNC since the migration of ethaline to the BioeGel surface could be reduced in a more reinforced network (Figure S1).

In addition, the BioeGels adhesion on different surfaces (Teflon, steel, wood, polypropylene, and glass) was measured, observing tackiness and energy of adhesion values in the order of those obtained for porcine skin (Figure 4D and Table S1). These adhesion data display slight variations between the different materials except for the glass, where larger tackiness and smaller adhesion energy were recorded. This smaller adhesion energy could be attributed to the rigidity of the glass. The fact that the BioeGels can adhere to different surfaces extends their range of applications.
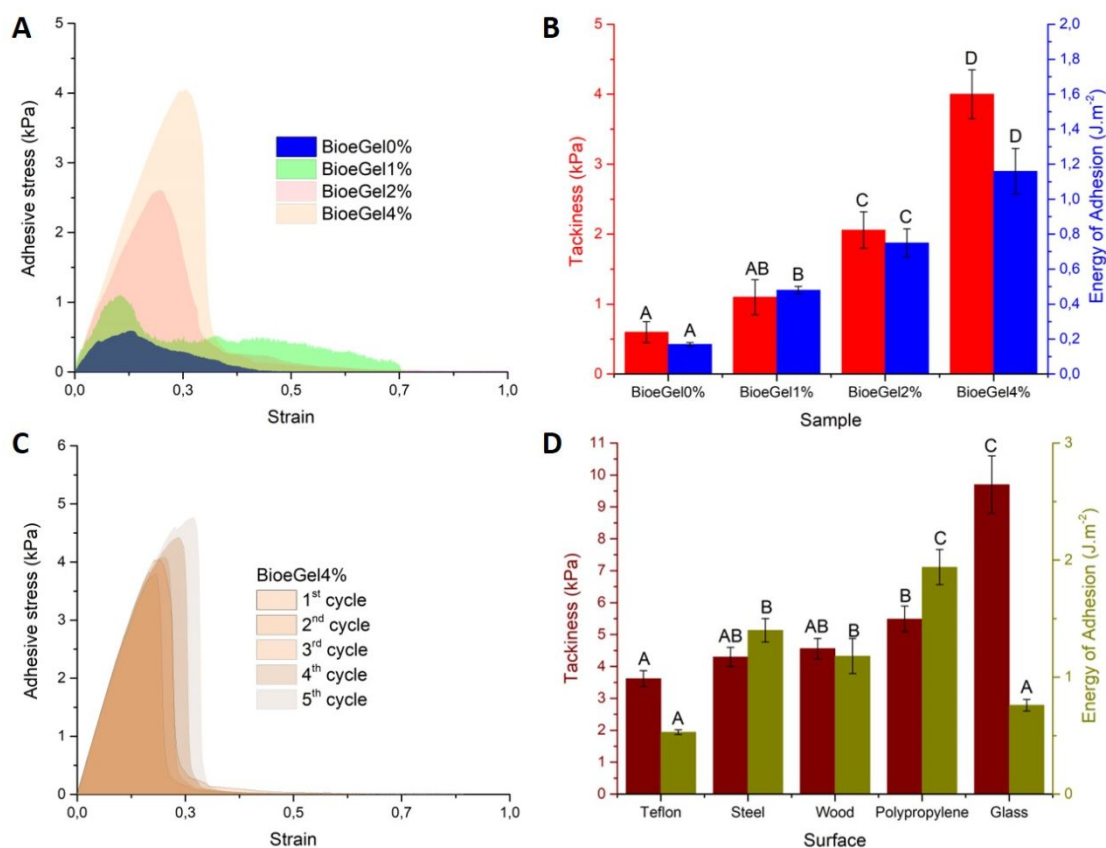
Figure 4. A) Adhesive stress vs. strain curves of the BioeGels. **B)** Tackiness (red column) and adhesion energy (blue column) values of BioeGel. **C)** Cyclic adhesive stress vs. strain curves of the prepared BioeGel4%. **D)** Tackiness (brown column) and adhesion energy (gold column) values in different surfaces of BioeGel4%. Two bar values with the same letter are not significantly different (p ≥ 0.05) according to Tukey's test.

Moreover, the viscoelastic properties of the as-prepared BioeGels were studied by small amplitude oscillatory shear. Figure 5A shows the storage modulus (G') as a function of the deformation amplitude in the range of 0.1 to 100%. BioeGel0% exhibited high modulus, and after adding 1 wt% of TA@CNC in BioeGel1%, it decreased to the lowest elasticity. Then, the subsequent addition of 2 and 4 wt% of TA@CNC produces a recovery of the original modulus. Considering that G' is

directly related to the gel crosslinking density, which in turn is primarily defined by the number of triple helices associations in the network, these results suggest that low TA@CNC contents somehow interfere with the formation of these gelatin helical bundles. Then, the recovery of G' with the further addition of TA@CNC is probably due to new physical crosslinking points, where flexible gelatin chains wrap onto the rigid nanocrystals by extensive H-bonding.
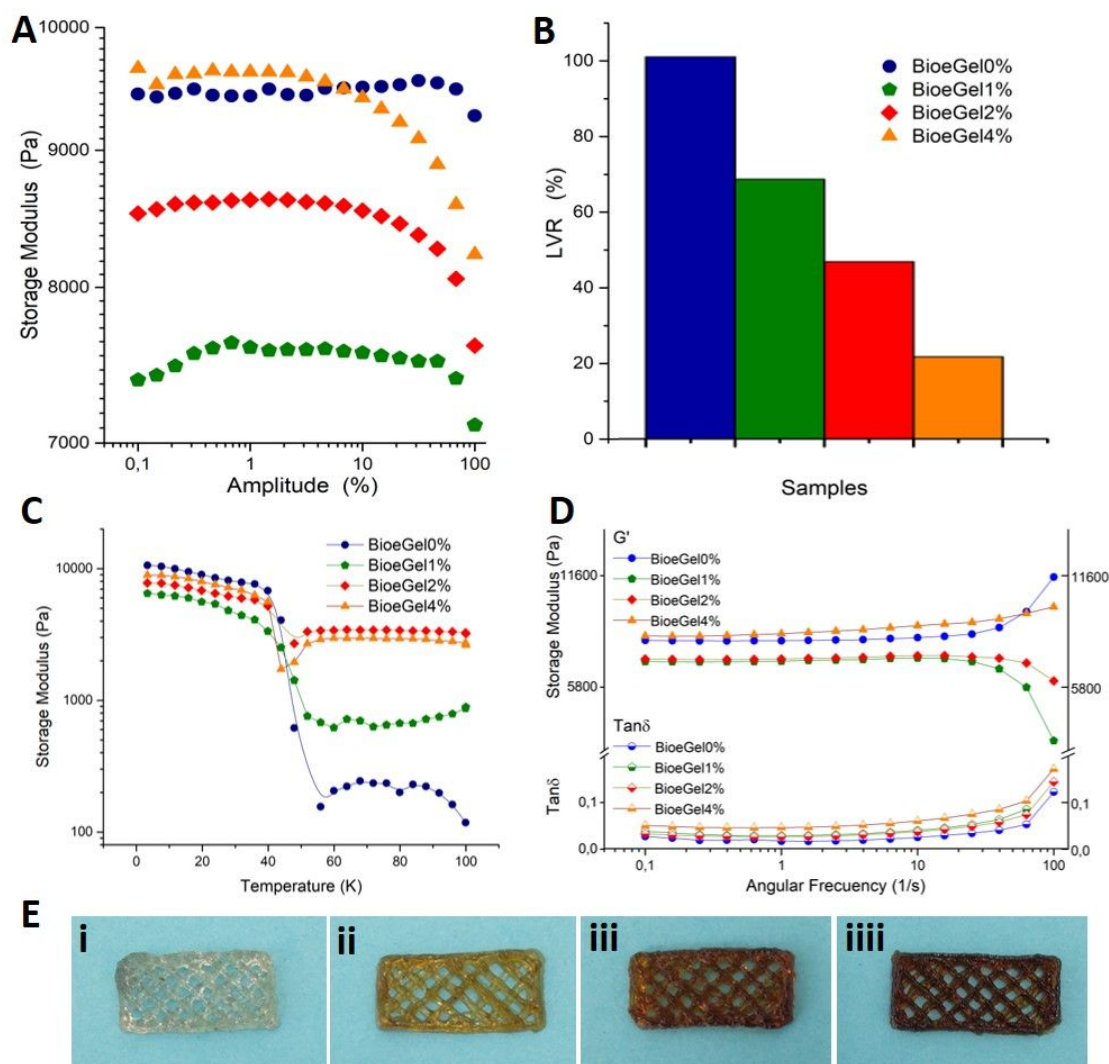
Figure 5. A) Storage modulus as a function of the amplitude of deformation. **B)** Linear viscoelastic range (LVR) for BioeGel samples. **C)** Storage modulus versus temperature obtained from DMTA of BioeGel samples. **D)** Storage modulus and Tand as a function of angular frequency for different BioeGel samples. **E)** 3D printing by hot extrusion at mild temperature (37 °C) of BioeGel0% **(i)**, BioeGel1% **(ii)**, BioeGel2% **(iii)** and BioeGel4% **(iiii)**.

For the application of BioeGels as wearable sensors, a lower elastic modulus is preferable to form mechanically compliant interfaces with the skin. Furthermore, the LVR of BioeGels should be considered to avoid permanent deformation after flexion or stretching during movement detection. Figure 5B shows the LVR for the BioeGels, and this parameter decrease after the addition of growing quantities of TA@CNC. The thermal gel-to-sol transitions were found at temperatures above 40°C, and after that, the elasticity significantly decreased for BioeGel0%, 50 times at 55°C (Figure 5C). Interestingly, TA@CNC improves the thermal stability and the elasticity after transitioning since G' only decreases 2, 2, and 6 times for BioeGel 2, 4, and 1%, respectively. Frequency sweeps confirmed that BioeGels0% and 4% are more elastic than 1% and 2% with a practically null variation under different frequencies, indicating a stable physically crosslinked network (Figure 5D). Tan δ values indicated in all cases that elastic moduli were about 20 times higher than the viscous moduli, and considering the samples set, BioeGel0% presented the highest elastic solid features.

An attractive feature of the as-prepared BioeGels is their capability to be 3D-impressed by the melting solidification printing process (MESO-PP) due to the solid-like behavior below ≈55 °C according to the rheological studies. As shown in Figure

5E, the 3D-printed Bioegels at 37°C kept the shape and patterns of the 3D design input. The results of 3D printability parameters described in the method section are shown in Table 1. Independently of the content of TA@CNC added to the BioeGels, all scaffolds have average I (for all directions) and Pp values around 100% ± 10 and 1 ± 0.1, respectively. These data conclude that the 3D-printed BioeGels have printability indexes that vary around 10% compared to the design model, indicating a very well printability feature of the samples. Besides, the addition of TA@CNC to BioeGsels does not significantly modify the printability indexes, keeping them at acceptable values. It is highlighted that the irregularity in the Z direction of a scaffold is an essential index of printability, the fact that I_Z values of BioeGels vary around 10% compared to the design model, reinforces the excellent printability of these BioeGels and opens the gates for using them as ionic bioinks.[57]

Table 1. Values of I for X, Y, and Z directions and Pp

	BioeGel0%	BioeGel1%	BioeGel2%	BioeGel4%
I_X	100.0±5.2[A]	102.1±6.1[a]	106.9±3.9 [a]	109.7±8.1 [a]
I_Y	97.4±4.9 [A]	103.7±5.7 [a]	105.3±3.1 [a]	108.9±7.2 [a]
I_Z	99.1±9.8 [A]	96.4±5.7 [a]	103.9±5.2 [a]	96.8±6.9 [a]
P_p	1.03±0.1 [A]	1.01±0.1 [a]	1.2±0.2 [a]	1.01±0.1 [a]

Two values in the same row followed by the same letter are not different (p≥0.05) according to the Tukey test.

Taking into account the flexion-extension of the index finger with respect to the back of the hand before (5°) and after (90°) grasping a small ball (Figure 6Ai),[44] the capabilities of BioeGels as motion sensors were tested by recording the specific

conductivity (k) when changing the bending angle between 5° and 90° in a regular close loop controlled by a servomotor and microcontroller (Figure 6Aii). Figure 6Aiii shows a representative cycle of the bending angle for the BioeGel2% sample, where the initial values of k are higher at the relaxed position, that is at 5°. After that, k values begin to decrease as the angle varies from 5° to 90° until reaching minimum values of k at 90° (during the highest stretching of the gel). Finally, k increase again in the transition from 90° to 5° (Video S1 shows 2 cycles of bending). The fact that the k values decrease as the bending angle increases is a reasonable result and is due to the area change (estimated as 1.5% according to eq. 4) of the BioeGel that restricts the ionic conductivity during the flexion movement.[58] The values of conductivity ($\frac{1}{R}$) for each BioeGel taken every 25 seconds along the 50 bending cycles are shown in Table S2 of the SI.
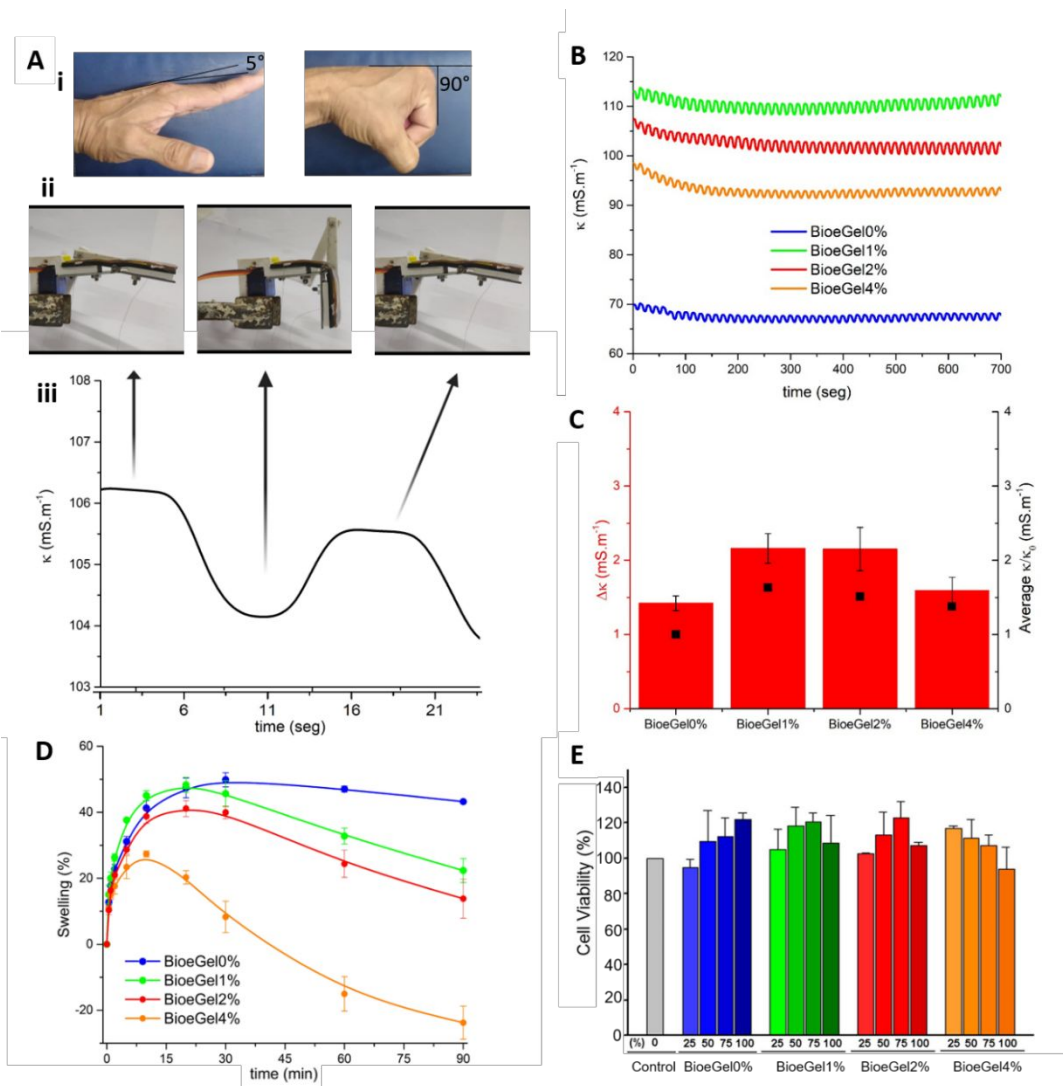
Figure 6. A. Flexion-extension movement of the index finger with respect to the back of the hand **(i)**; flexion-extension movement of servomotor and microcontroller **(ii);** a representative cycle of bending angle for BioeGel2% **(iii)**. **B.** K values of BioeGels along 50 cycles of movement between 5°-90°-5°. **C**. Average ΔK values of all BioeGels for 50 cycles of movement. **D)** Water swelling degree (%) vs. time for the different BioeGels. **E)** Cytotoxicity testing of BioeGel extracts on MRC-5 human fibroblast cells by MTT assay. The viability of the cells exposed only to the culture medium was set at 100% (Control, grey bar).

The k values of the BioeGels loaded with different contents of TA@CNC over 50 bending cycles are shown in Figure 6B, where smooth signals with low noise and excellent reproducibility during the test are observed for all samples. As expected, BioeGel0% presented a predictable conductivity of 72 mS.m^{-1} according to Manning's theory, considering that the eutectic mixture and collagen dielectric constants are the main ones responsible for ionic conductivity. Furthermore, it was found that similar ionic gels exhibited conductivities in the same order of magnitude as BioeGels.[59] Interestingly, the k values of BioeGels loaded with TA@CNC yielded conductivities higher than BioeGel0%. In this sense, previous works suggested that the addition of CNC as well as a crosslinker as TA can enhance the ionic conductivity.[60,61] Note that the k value for BioeGel4% is lower than BioeGel1% and 2%, which could be explained by the effect of densely packed TA@CNC at high concentration, hindering the ionic conductivity.[62] In this regard, the average values of k after TA@CNC addition show a peak response by the effects related to conductivity-dependent concentration of a weak electrolyte like TA (according to Ostwald's dilution law), and the contribution in the dielectric constant after TA@CNC addition giving a decreasing of the activity coefficient γ_i.

The sensitivity of all BioeGels to detect the change in the bending angle was obtained by calculating the average delta of k (Δk), the average difference between k during 50 bending cycles at 5° and 90° (Figure 6C). In the first inspection, BioeGel1% and BioeGel 2% show similar Δk values around 2.2 mS.m^{-1} without significative differences between them, while BioeGel0% and BioeGel4% have a Δk average of 1.5 mS.m^{-1}, indicating to be less sensitive to movement changes than

BioeGel1% and BioeGel2%. This fact is probably due to the TA@CNC effect on ion conductivity, as mentioned above. Furthermore, we consider that this variation is closely related to the average k values and the decreasing BioeGel area during the stretching in the bending position. Thus, we calculated the ratio of conductivities (k/k_0) with respect to the BioeGel0% conductivity (k_0) (Figure 6C, black squares). The results indicate that the conductivity ratios are comparable with the bar data of Δk, showing the same tendency, which supports our hypothesis. Despite these k variations and the mechanical differences observed in the tensile tests, it is highlighted that all BioeGels have relatively small standard deviations values of around 5% (Figure 6C, error black bars), indicating that over the 50 bending cycles, their ability to detect movement changes is practically unalterable, making the as-prepared BioeGels robust candidates as motion sensors.

Given the hydrophilic nature of ethaline and gelatin, it is expected that the BioeGels are hygroscopic materials. Therefore, the stability in water of these ionic materials is a key parameter, considering their potential application as skin-conformal sensors. The water uptake ($\%S$) behavior of the BioeGels is shown in Figure 6D. The $\%S$ curves show 2 stages; the first is a gradual increment of the water sorption over time until it reaches a maximum value at a specific point depending on the TA@CNC content. As the concentration of TA@CNC increases, the $\%S$ average values varied from 49 to 28% for BioeGels0% and 4%, and the maximum swelling value is achieved at 30 and 10 min, respectively. This trend is due to the presence of the phenolic compound in TA@CNC that can promote multiple H-bond interactions, forming a more compact, physically crosslinked network.[63] The second stage start

after BioeGels reach the maximum values of $\%S$ and is evidenced by a loss of soluble material, being more noticeable as the amonut of TA@CNC increases. This behavior is probably because of the water affinity of TA@CNC increasing the amount of soluble matter, which in turn, speeds up the gel dissolution.

The potential use and safety of these BioeGels as biocompatible materials were also evaluated by cell viability test. MRC-5 human fibroblast cells were exposed to increasing concentrations (25% to 100%) of BioeGels extracts for 24 h. BioeGels cytotoxicity was assessed by determining the viability of cells by MTT, a mitochondrial assay. The viability of the cells exposed only to the culture medium was set at 100% to compare with the responses of the BioeGels extracts. The results shown in Figure 6E indicate that the extracts from BioeGels without TA@CNC or loaded with 1, 2, and 4 wt%, when used at 100% or dilution series of the original extract (75% to 25%), exert no cytotoxic effects on MRC-5 cells. Moreover, the cellular viability under all the conditions evaluated was above 90%, so the material was determined to be non-cytotoxic according to ISO 10993-5 and ISO 10993-12, which state that a reduction in viability greater than 30% is considered a cytotoxic effect. Hence, our findings show that the synthesized BioeGels could be considered non-cytotoxic under the given conditions, determining them as suitable for biomedical and related applications.

Finally, we test the biodegradability performance of the BioeGels by soil burial experiments for 6 days in controlled composting conditions. After this period, all BioeGels had a weight loss higher than 60% reaching up to 90% for the BioeGel2%, indicating that they are readily biodegradables (Figure S2).[64,65]

Conclusions

In this work, we have synthesized a new type of natural and biocompatible nanocomposite eutectogel by combining the properties of porcine gelatin, ethaline eutectic mixture (choline chloride/ ethylene glycol), and tannic acid-coated cellulose nanocrystals (TA@CNC). The addition of TA@CNC at low concentration (1 or 2 wt%) acts as a reinforcer agent by hydrogen bonding interactions, making the BioeGels more resistant and flexible and with less water-sensitive behavior at specific nanocrystal concentrations. For the highest TA@CNC content analyzed (4 wt%), the mechanical properties of BioeGels exhibit a detriment due to the presence of TA@CNC agglomerates that impair, to some extent, their reinforcer mechanism probably based on energy dissipation by gelatin chain/nanocrystals interfacial debonding. The BioeGels show the capability to be 3D-printed by MESO-PP with excellent values of printability index, independently of the TA@CNC concentration added. The as-prepared BioeGels can sense the changes in body movements by varying the specific conductivity values during bending-extension steps. The addition of TA@CNC improves the ionic conductivity of the BioeGels until 2 wt% by the effects of the TA electrolyte, whereas at the highest TA@CNC concentration, the specific conductivity slightly decreases due to the densely packed network formed. Finally, these BioeGels have proven to be good candidates for bioelectronics since cell viability data showed that all materials could be considered non-cytotoxic. All in all, we demonstrated that TA@CNC as dynamic and rigid nanofillers could significantly enhance the mechanical and viscoelastic performance of biopolymers

eutectogels, expanding the applicability of this emerging family of low-cost ionic materials to innovative realms like biodegradable electronics.

Supporting Information

Conductivity data; Cyclic adhesion data; Tackiness and Energy of Adhesion data; Biodegradability results; Video showing a motion sensor working in real time (MP4 file).

Author Contributions

P.A.M designed and performed the research and wrote the manuscript; M.R.R performed the rheological test, analyzed and co-wrote the manuscript; M.M.M performed the cell viability assay; J.P.R performed 3D printed assay; M.L.P and A.G designed the research, co-wrote the manuscript and provided overall guidance.

Notes

 The authors declare no competing financial interest

Acknowledge

References

(1)   Yu, D.; Xue, Z.; Mu, T. Eutectics: Formation, Properties, and Applications. *Chemical Society Reviews*. 2021. https://doi.org/10.1039/d1cs00404b.

(2)   Perna, F. M.; Vitale, P.; Capriati, V. Deep Eutectic Solvents and Their Applications as Green Solvents. *Current Opinion in Green and Sustainable Chemistry*. 2020. https://doi.org/10.1016/j.cogsc.2019.09.004.

(3)   Shaibuna, M.; Theresa, L. V.; Sreekumar, K. Neoteric Deep Eutectic Solvents: History, Recent Developments, and Catalytic Applications. *Soft Matter* **2022**, *18* (14), 2695–2721. https://doi.org/10.1039/D1SM01797G.

(4)   Tomé, L. C.; Mecerreyes, D. Emerging Ionic Soft Materials Based on Deep Eutectic Solvents. *Journal of Physical Chemistry B*. 2020. https://doi.org/10.1021/acs.jpcb.0c04769.

(5)   Wang, J.; Zhang, S.; Ma, Z.; Yan, L. Deep Eutectic Solvents Eutectogels: Progress and Challenges. *Green Chem. Eng.* **2021**, *2* (4), 359–367. https://doi.org/10.1016/j.gce.2021.06.001.

(6)   Wang, Y.; Wang, J.; Ma, Z.; Yan, L. A Highly Conductive, Self-Recoverable, and Strong Eutectogel of a Deep Eutectic Solvent with Polymer Crystalline Domain Regulation. *ACS Appl. Mater. Interfaces* **2021**, *13* (45), 54409–54416. https://doi.org/10.1021/acsami.1c17442.

(7)   Zhang, H.; Tang, N.; Yu, X.; Li, M. H.; Hu, J. Strong and Tough Physical Eutectogels Regulated by the Spatiotemporal Expression of Non-Covalent Interactions. *Adv. Funct. Mater.* **2022**.

https://doi.org/10.1002/adfm.202206305.

(8)   Feng, Y.; Yu, J.; Sun, D.; Dang, C.; Ren, W.; Shao, C.; Sun, R. Extreme Environment-Adaptable and Fast Self-Healable Eutectogel Triboelectric Nanogenerator for Energy Harvesting and Self-Powered Sensing. *Nano Energy* **2022**, *98* (February), 107284. https://doi.org/10.1016/j.nanoen.2022.107284.

(9)   Wan, Y.; Huang, S.; Sun, Y.; Zhu, H.; Zheng, Q.; Zhang, Q.; Zhu, S. Superstrong yet Water-Detachable Eutectogel Adhesives. *Chem. Eng. J.* **2022**, *442* (P2), 136289. https://doi.org/10.1016/j.cej.2022.136289.

(10)   Wang, J.; Deng, Y.; Ma, Z.; Wang, Y.; Zhang, S.; Yan, L. Lignin Promoted the Fast Formation of a Robust and Highly Conductive Deep Eutectic Solvent Ionic Gel at Room Temperature for a Flexible Quasi-Solid-State Supercapacitor and Strain Sensors. *Green Chem.* **2021**. https://doi.org/10.1039/d1gc01512e.

(11)   Wang, J.; Ma, Z.; Wang, Y.; Shao, J.; Yan, L. Ultra-Stretchable, Self-Healing, Conductive, and Transparent PAA/DES Ionic Gel. *Macromol. Rapid Commun.* **2021**, *42* (2), 1–5. https://doi.org/10.1002/marc.202000445.

(12)   Hong, S.; Yuan, Y.; Liu, C.; Chen, W.; Chen, L.; Lian, H.; Liimatainen, H. A Stretchable and Compressible Ion Gel Based on a Deep Eutectic Solvent Applied as a Strain Sensor and Electrolyte for Supercapacitors. *J. Mater. Chem. C* **2020**. https://doi.org/10.1039/c9tc05913j.

(13)   Zhou, Q.; Dong, L.; Wu, J.; Shi, Y.; Feng, X.; Lu, X.; Zhu, J.; Mu, L. Versatile

Ionic Gel Driven by Dual Hydrogen Bond Networks: Toward Advanced Lubrication and Self-Healing. *ACS Appl. Polym. Mater.* **2021**, *3* (11), 5932–5941. https://doi.org/10.1021/acsapm.1c01189.

(14) Fan, K.; Wei, W.; Zhang, Z.; Liu, B.; Feng, W.; Ma, Y.; Zhang, X. Highly Stretchable, Self-Healing, and Adhesive Polymeric Eutectogel Enabled by Hydrogen-Bond Networks for Wearable Strain Sensor. *Chem. Eng. JournalJournal* **2022**, *449* (July), 137878. https://doi.org/10.2139/ssrn.4092246.

(15) Wang, S.; Cheng, H.; Yao, B.; He, H.; Zhang, L.; Yue, S.; Wang, Z.; Ouyang, J. Self-Adhesive, Stretchable, Biocompatible, and Conductive Nonvolatile Eutectogels as Wearable Conformal Strain and Pressure Sensors and Biopotential Electrodes for Precise Health Monitoring. *ACS Appl. Mater. Interfaces* **2021**. https://doi.org/10.1021/acsami.1c04671.

(16) Chen, T.; Luo, R.; Liu, Y.; Ma, L.; Li, Z.; Tao, C.; Yang, S.; Wang, J. Two-Dimensional Nanosheet-Enhanced Waterborne Polyurethane Eutectogels with Ultrastrength and Superelasticity for Sensitive Strain Sensors. *ACS Appl. Mater. Interfaces* **2022**, *14* (35), 40276–40285. https://doi.org/10.1021/acsami.2c08331.

(17) Bianchi, M. B.; Zhang, C.; Catlin, E.; Sandri, G.; Calderón, M.; Larrañeta, E.; Donnelly, R. F.; Picchio, M. L.; Paredes, A. J. Bioadhesive Eutectogels Supporting Drug Nanocrystals for Long-Acting Delivery to Mucosal Tissues. *Mater. Today Bio* **2022**, *17* (October).

https://doi.org/10.1016/j.mtbio.2022.100471.

(18) Picchio, M. L.; Gallastegui, A.; Casado, N.; Lopez-Larrea, N.; Marchiori, B.;

del Agua, I.; Criado-Gonzalez, M.; Mantione, D.; Minari, R. J.; Mecerreyes,

D. Mixed Ionic and Electronic Conducting Eutectogels for 3D-Printable

Wearable Sensors and Bioelectrodes. *Adv. Mater. Technol.* **2022**, *2101680*.

https://doi.org/10.1002/admt.202101680.

(19) Nyamayaro, K.; Keyvani, P.; D'Acierno, F.; Poisson, J.; Hudson, Z. M.;

Michal, C. A.; Madden, J. D. W.; Hatzikiriakos, S. G.; Mehrkhodavandi, P.

Toward Biodegradable Electronics: Ionic Diodes Based on a Cellulose

Nanocrystal-Agarose Hydrogel. *ACS Appl. Mater. Interfaces* **2020**, *12* (46),

52182–52191. https://doi.org/10.1021/acsami.0c15601.

(20) Baumgartner, M.; Hartmann, F.; Drack, M.; Preninger, D.; Wirthl, D.;

Gerstmayr, R.; Lehner, L.; Mao, G.; Pruckner, R.; Demchyshyn, S.; Reiter,

L.; Strobel, M.; Stockinger, T.; Schiller, D.; Kimeswenger, S.; Greibich, F.;

Buchberger, G.; Bradt, E.; Hild, S.; Bauer, S.; Kaltenbrunner, M. Resilient yet

Entirely Degradable Gelatin-Based Biogels for Soft Robots and Electronics.

Nat. Mater. **2020**, *19* (10), 1102–1109. https://doi.org/10.1038/s41563-020-

0699-3.

(21) Depoorter, J.; Mourlevat, A.; Sudre, G.; Morfin, I.; Prasad, K.; Serghei, A.;

Bernard, J.; Fleury, E.; Charlot, A. Fully Biosourced Materials from

Combination of Choline Chloride-Based Deep Eutectic Solvents and Guar

Gum. *ACS Sustain. Chem. Eng.* **2019**.

https://doi.org/10.1021/acssuschemeng.9b04228.

(22)   Zeng, C.; Zhao, H.; Wan, Z.; Xiao, Q.; Xia, H.; Guo, S. Highly Biodegradable,

Thermostable Eutectogels Prepared by Gelation of Natural Deep Eutectic

Solvents Using Xanthan Gum: Preparation and Characterization. *RSC Adv.*

2020. https://doi.org/10.1039/d0ra03390a.

(23)   Xia, H.; Ren, M.; Zou, Y.; Qin, S.; Zeng, C. Novel Biocompatible

Polysaccharide-Based Eutectogels with Tunable Rheological, Thermal, and

Mechanical Properties: The Role of Water. *Molecules* **2020**.

https://doi.org/10.3390/molecules25153314.

(24)   Ma, Z.; Wang, J.; Deng, Y.; Wang, Y.; Yan, L. Synthesis of Highly Ion-

Conductive Lignin Eutectogels in a Ternary Deep Eutectic Solvent and

Nitrogen-Doped 3D Hierarchical Porous Carbons for Supercapacitors.

Biomacromolecules **2021**, *22* (10), 4181–4190.

https://doi.org/10.1021/acs.biomac.1c00706.

(25)   Tian, Y.; Sun, D. W.; Xu, L.; Fan, T. H.; Zhu, Z. Bio-Inspired Eutectogels

Enabled by Binary Natural Deep Eutectic Solvents (NADESs): Interfacial

Anti-Frosting, Freezing-Tolerance, and Mechanisms. *Food Hydrocoll.* **2022**,

128 (January), 107568. https://doi.org/10.1016/j.foodhyd.2022.107568.

(26)   Owyeung, R. E.; Sonkusale, S. R.; Panzer, M. J. Influence of Hydrogen Bond

Donor Identity and Intentional Water Addition on the Properties of Gelatin-

Supported Deep Eutectic Solvent Gels. *J. Phys. Chem. B* **2020**, *124* (28),

5986–5992. https://doi.org/10.1021/acs.jpcb.0c03361.

(27) Qin, H.; Owyeung, R. E.; Sonkusale, S. R.; Panzer, M. J. Highly Stretchable and Nonvolatile Gelatin-Supported Deep Eutectic Solvent Gel Electrolyte-Based Ionic Skins for Strain and Pressure Sensing. *J. Mater. Chem. C* **2019**. https://doi.org/10.1039/c8tc05918g.

(28) Agieienko, V.; Buchner, R. Is Ethaline a Deep Eutectic Solvent? *Phys. Chem. Chem. Phys.* **2022**, *24* (9), 5265–5268. https://doi.org/10.1039/d2cp00104g.

(29) Silva, L. P.; Martins, M. A. R.; Conceição, J. H. F.; Pinho, S. P.; Coutinho, J. A. P. Eutectic Mixtures Based on Polyalcohols as Sustainable Solvents: Screening and Characterization. *ACS Sustain. Chem. Eng.* **2020**, *8* (40), 15317–15326. https://doi.org/10.1021/acssuschemeng.0c05518.

(30) Lai, C. W.; Yu, S. S. 3D Printable Strain Sensors from Deep Eutectic Solvents and Cellulose Nanocrystals. *ACS Appl. Mater. Interfaces* **2020**, *12* (30), 34235–34244. https://doi.org/10.1021/acsami.0c11152.

(31) Cui, C.; Shao, C.; Meng, L.; Yang, J. High-Strength, Self-Adhesive, and Strain-Sensitive Chitosan/Poly(Acrylic Acid) Double-Network Nanocomposite Hydrogels Fabricated by Salt-Soaking Strategy for Flexible Sensors. *ACS Appl. Mater. Interfaces* **2019**. https://doi.org/10.1021/acsami.9b15817.

(32) Shao, C.; Meng, L.; Wang, M.; Cui, C.; Wang, B.; Han, C.-R.; Xu, F.; Yang, J. Mimicking Dynamic Adhesiveness and Strain-Stiffening Behavior of Biological Tissues in Tough and Self-Healable Cellulose Nanocomposite Hydrogels. *ACS Appl. Mater. Interfaces* **2019**, *11* (6), 5885–5895.

https://doi.org/10.1021/acsami.8b21588.

(33) Carnicero, A.; González, A.; Dalosto, S. D.; Passeggi, M. C. G.; Minari, R. J.;

Alvarez Igarzabal, C. I.; Martinelli, M.; Picchio, M. L. Ascidian-Inspired

Supramolecular Cellulose Nanocomposite Hydrogels with Antibacterial

Activity. *ACS Biomater. Sci. Eng.* **2022**, *8* (11), 5027–5037.

https://doi.org/10.1021/acsbiomaterials.2c00935.

(34) Shao, C.; Wang, M.; Meng, L.; Chang, H.; Wang, B.; Xu, F.; Yang, J.; Wan,

P. Mussel-Inspired Cellulose Nanocomposite Tough Hydrogels with

Synergistic Self-Healing, Adhesive, and Strain-Sensitive Properties. *Chem.*

Mater. **2018**, *30* (9), 3110–3121.

https://doi.org/10.1021/acs.chemmater.8b01172.

(35) Yang, S.; Zhang, Y.; Wang, T.; Sun, W.; Tong, Z. Ultrafast and

Programmable Shape Memory Hydrogel of Gelatin Soaked in Tannic Acid

Solution. *ACS Appl. Mater. Interfaces* **2020**, *12* (41), 46701–46709.

https://doi.org/10.1021/acsami.0c13531.

(36) Xu, R.; Ma, S.; Lin, P.; Yu, B.; Zhou, F.; Liu, W. High Strength Astringent

Hydrogels Using Protein as the Building Block for Physically Cross-Linked

Multi-Network. *ACS Appl. Mater. Interfaces* **2018**, *10* (9), 7593–7601.

https://doi.org/10.1021/acsami.7b04290.

(37) Han, Y.; Lin, Z.; Zhou, J.; Yun, G.; Guo, R.; Richardson, J. J.; Caruso, F.

Polyphenol-Mediated Assembly of Proteins for Engineering Functional

Materials. *Angew. Chemie Int. Ed.* **2020**, *59* (36), 15618–15625.

https://doi.org/10.1002/anie.202002089.

(38) Ma, S.; Lee, H.; Liang, Y.; Zhou, F. Astringent Mouthfeel as a Consequence of Lubrication Failure. *Angew. Chemie Int. Ed.* **2016**, *55* (19), 5793–5797. https://doi.org/10.1002/anie.201601667.

(39) *PubChem-National Center for Biotechnology Information*. https://pubchem.ncbi.nlm.nih.gov/compound/16129778#section=Chemical-and-Physical-Properties (accessed 2023-02-25).

(40) Tan, Z.; Peng, Y.; Liu, J.; Yang, Y.; Zhang, Z.; Chen, Z.; Mao, B.; Yan, J. An In Situ Scanning Tunneling Microscopy Study on the Electrochemical Interface between Au(111) and Ethaline Deep Eutectic Solvent. *ChemElectroChem* **2020**, *7* (22), 4601–4605. https://doi.org/10.1002/celc.202001264.

(41) González, A.; Gastelú, G.; Barrera, G. N.; Ribotta, P. D.; Álvarez Igarzabal, C. I. Preparation and Characterization of Soy Protein Films Reinforced with Cellulose Nanofibers Obtained from Soybean By-Products. *Food Hydrocoll.* **2019**, *89*, 758–764. https://doi.org/10.1016/j.foodhyd.2018.11.051.

(42) ASTM. Standard Test Method for Tensile Properties of Thin Plastic Sheeting; 2002; p 9. https://doi.org/10.1520/D0882-02.

(43) Naghieh, S.; Sarker, M.; Sharma, N. K.; Barhoumi, Z.; Chen, X. Printability of 3D Printed Hydrogel Scaffolds: Influence of Hydrogel Composition and Printing Parameters. *Appl. Sci.* **2019**, *10* (1), 292. https://doi.org/10.3390/app10010292.

1
2
3
4	(44)	Chen Chen, F.; Appendino, S.; Battezzato, A.; Favetto, A.; Mousavi, M.;
5
6		Pescarmona, F. Constraint Study for a Hand Exoskeleton: Human Hand
7
8		Kinematics and Dynamics. *J. Robot.* **2013**, *2013*, 1–17.
9
10		https://doi.org/10.1155/2013/910961.
11
12
13	(45)	*Biological evaluation of medical devices — Part 5: Tests for in vitro*
14
15		*cytotoxicity*. https://www.iso.org/standard/36406.html (accessed 2023-02-23).
16
17
18	(46)	*Biological evaluation of medical devices — Part 12: Sample preparation and*
19
20		*reference materials*. https://www.iso.org/standard/75769.html (accessed
21
22
23		2023-02-23).
24
25
26	(47)	Srivastava, G. K.; Alonso-Alonso, M. L.; Fernandez-Bueno, I.; Garcia-
27
28		Gutierrez, M. T.; Rull, F.; Medina, J.; Coco, R. M.; Pastor, J. C. Comparison
29
30		between Direct Contact and Extract Exposure Methods for PFO Cytotoxicity
31
32
33		Evaluation. *Sci. Rep.* **2018**, *8* (1), 1425. https://doi.org/10.1038/s41598-018-
34
35		19428-5.
36
37
38	(48)	González, A.; Alvarez Igarzabal, C. I. Soy Protein – Poly (Lactic Acid) Bilayer
39
40		Films as Biodegradable Material for Active Food Packaging. *Food Hydrocoll.*
41
42
43		**2013**, *33* (2), 289–296. https://doi.org/10.1016/j.foodhyd.2013.03.010.
44
45
46	(49)	Sivrikaya, S. A Novel Vortex-Assisted Liquid Phase Microextraction Method
47
48		for Parabens in Cosmetic Oil Products Using Deep Eutectic Solvent. *Int. J.*
49
50		*Environ. Anal. Chem.* **2019**, *99* (15), 1575–1585.
51
52
53		https://doi.org/10.1080/03067319.2019.1625345.
54
55
56	(50)	Ibrahim, R. K.; Hayyan, M.; AlSaadi, M. A.; Ibrahim, S.; Hayyan, A.; Hashim,
57
58
59

M. A. Physical Properties of Ethylene Glycol-Based Deep Eutectic Solvents. *J. Mol. Liq.* **2019**, *276*, 794–800. https://doi.org/10.1016/j.molliq.2018.12.032.

(51) Hashim, D. M.; Man, Y. B. C.; Norakasha, R.; Shuhaimi, M.; Salmah, Y.; Syahariza, Z. A. Potential Use of Fourier Transform Infrared Spectroscopy for Differentiation of Bovine and Porcine Gelatins. *Food Chem.* **2010**, *118* (3), 856–860. https://doi.org/10.1016/j.foodchem.2009.05.049.

(52) Xu, X.; Liu, F.; Jiang, L.; Zhu, J. Y.; Haagenson, D.; Wiesenborn, D. P. Cellulose Nanocrystals vs. Cellulose Nanofibrils: A Comparative Study on Their Microstructures and Effects as Polymer Reinforcing Agents. *ACS Appl. Mater. Interfaces* **2013**, *5* (8), 2999–3009. https://doi.org/10.1021/am302624t.

(53) Li, Z.; Yu, C.; Kumar, H.; He, X.; Lu, Q.; Bai, H.; Kim, K.; Hu, J. The Effect of Crosslinking Degree of Hydrogels on Hydrogel Adhesion. *Gels* **2022**, *8* (10), 682. https://doi.org/10.3390/gels8100682.

(54) Picchio, M. L.; Gallastegui, A.; Casado, N.; Lopez-Larrea, N.; Marchiori, B.; del Agua, I.; Criado-Gonzalez, M.; Mantione, D.; Minari, R. J.; Mecerreyes, D. Mixed Ionic and Electronic Conducting Eutectogels for 3D-Printable Wearable Sensors and Bioelectrodes. *Adv. Mater. Technol.* **2022**, *7* (10), 2101680. https://doi.org/10.1002/admt.202101680.

(55) Pailler-Mattéi, C.; Zahouani, H. Analysis of Adhesive Behaviour of Human Skin in Vivo by an Indentation Test. *Tribol. Int.* **2006**, *39* (1), 12–21. https://doi.org/10.1016/j.triboint.2004.11.003.

(56) Pailler-Mattéi, C.; Zahouani, H. Study of Adhesion Forces and Mechanical Properties of Human Skin in Vivo. *J. Adhes. Sci. Technol.* **2004**, *18* (15–16), 1739–1758. https://doi.org/10.1163/1568561042708368.

(57) Naghieh, S.; Chen, X. Printability–A Key Issue in Extrusion-Based Bioprinting. *J. Pharm. Anal.* **2021**, *11* (5), 564–579. https://doi.org/10.1016/j.jpha.2021.02.001.

(58) Wang, L.; Xu, T.; Zhang, X. Multifunctional Conductive Hydrogel-Based Flexible Wearable Sensors. *TrAC Trends Anal. Chem.* **2021**, *134*, 116130. https://doi.org/10.1016/j.trac.2020.116130.

(59) Liu, C.; Qi, J.; He, B.; Zhang, H.; Ju, J.; Yao, X. Ionic Conductive Gels Based on Deep Eutectic Solvents. *Int. J. Smart Nano Mater.* **2021**, *12* (3), 337–350. https://doi.org/10.1080/19475411.2021.1972053.

(60) Kim, J.-H.; Shim, B. S.; Kim, H. S.; Lee, Y.-J.; Min, S.-K.; Jang, D.; Abas, Z.; Kim, J. Review of Nanocellulose for Sustainable Future Materials. *Int. J. Precis. Eng. Manuf. Technol.* **2015**, *2* (2), 197–213. https://doi.org/10.1007/s40684-015-0024-9.

(61) Calle-Gil, R.; Castillo-Martínez, E.; Carretero-González, J. Cellulose Nanocrystals in Sustainable Energy Systems. *Adv. Sustain. Syst.* **2022**, *6* (4), 2100395. https://doi.org/10.1002/adsu.202100395.

(62) Kim, J.-H.; Kim, J.-H.; Choi, E.-S.; Yu, H. K.; Kim, J. H.; Wu, Q.; Chun, S.-J.; Lee, S.-Y.; Lee, S.-Y. Colloidal Silica Nanoparticle-Assisted Structural Control of Cellulose Nanofiber Paper Separators for Lithium-Ion Batteries. *J.*

Power Sources **2013**, *242*, 533–540.

https://doi.org/10.1016/j.jpowsour.2013.05.142.

(63) Cao, N.; Fu, Y.; He, J. Mechanical Properties of Gelatin Films Cross-Linked,

Respectively, by Ferulic Acid and Tannin Acid. *Food Hydrocoll.* **2007**, *21* (4),

575–584. https://doi.org/10.1016/j.foodhyd.2006.07.001.

(64) Lapeña, D.; Errazquin, D.; Lomba, L.; Lafuente, C.; Giner, B. Ecotoxicity and

Biodegradability of Pure and Aqueous Mixtures of Deep Eutectic Solvents:

Glyceline, Ethaline, and Reline. *Environ. Sci. Pollut. Res.* **2021**, *28* (7),

8812–8821. https://doi.org/10.1007/s11356-020-11144-w.

(65) Martucci, J. F.; Ruseckaite, R. A. Biodegradation of Three-Layer Laminate

Films Based on Gelatin under Indoor Soil Conditions. *Polym. Degrad. Stab.*

2009, *94* (8), 1307–1313.

https://doi.org/10.1016/j.polymdegradstab.2009.03.018.

1
2
3
4
5
6
7
8
9
10
11
12
13
14
15
16
17
18
19
20
21
22
23
24
25
26
27
28
29
30
31
32
33
34
35
36
37
38
39
40
41
42
43
44
45
46
47
48
49
50
51
52
53
54
55
56
57
58
59
60

Table of Content